Design and Control of 6-DOF High-Precision Scan Stage with Gravity Canceller

Wataru Ohnishi[1], Hiroshi Fujimoto[1], Koichi Sakata[2], Kazuhiro Suzuki[2] and Kazuaki Saiki[2]

***Abstract*— High-precision scan stages are used for fabrication of integrated circuits, liquid crystal displays and so on. To fabricate such precise devices, not only stages position but also stages attitude needs to be controlled rapidly and precisely. In this paper, an experimental 6-degree-of-freedom (6-DOF) high-precision stage with a novel 6-DOF air bearing called "gravity canceller" is designed and fabricated. The 6-DOF stage consists of a fine stage and a coarse stage. The gravity canceller compensates for the fine stage's gravity and supports the fine stage without friction. This structure enables us to reduce heat which is generated close to the fine stage. For a 6-DOF control problem, attitude control is as important as translational control. Rotational motion, however, has nonlinearity and coupling arising from dynamics and kinematics which could degrade the attitude control performance. Therefore, in our past paper, our research group proposed a multi-input multi-output nonlinear feedforward attitude controller to compensate such problems. Experiments were performed to verify the effectiveness of the attitude controller by using the new experimental 6-DOF stage.**

I. Introduction

High-precision scan stages are implemented in manufacturing process for electronic devices such as integrated circuits and liquid crystal displays. To fabricate such precise devices, fast and precise control are required for not only stages position but also stages attitude [1]. Moreover, stages need to track 6-DOF reference trajectories considering surface geometry of wafers or flat panels [2].

To achieve high control performance, a contactless fine stage is desirable because this structure can remarkably reduce friction. This structure, however, needs gravity compensation. For this purpose, air bearing systems or magnetic levitation systems are often used [3][4]. Although magnetic levitation systems have advantages of vacuum compatibility, they also have a disadvantage of generating heat and difficulty of controlling stages compared to air bearing systems. The heat generated by coils could change characteristics of actuators and sensors, and lead to degrade positioning resolution [5]. On the other hand, due to simple structure, air bearing systems are lightweight and cost-effective compared to magnetic levitation systems. Because of these reasons, a novel 6-DOF air bearing called "gravity canceller" is exploited for our 6-DOF high-precision stage.

In this paper, a new experimental 6-DOF high-precision stage with gravity canceller is designed and fabricated. This stage consists of a fine stage and a coarse stage. The gravity canceller compensates for the fine stage's gravity and supports 6-DOF without friction. The fine stage is accelerated by voice coil motors (VCMs). This structure can reduce VCMs' required thrust because VCMs need not to compensate for the fine stage's gravity. Consequently, the heat generated close to the fine stage can be minimized.

For a 6-DOF fine stage control, not only translational

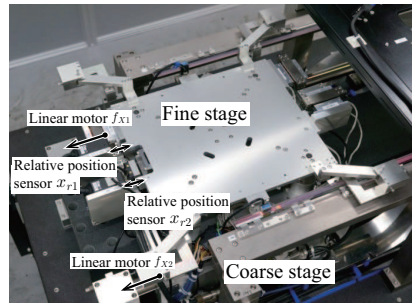

Fig. 1. Picture of the 6-DOF high-precision stage.

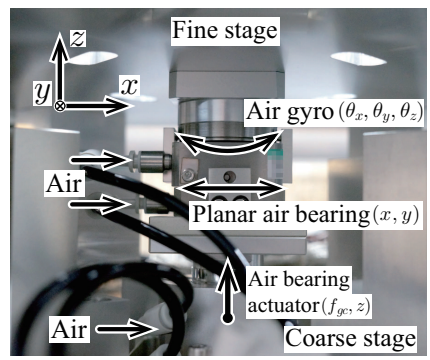

(a) Side view.

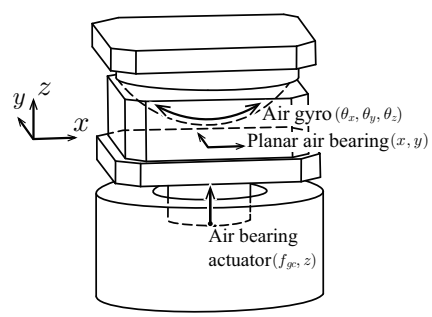

(b) Schematic.

Fig. 2. Structure of the gravity canceller.

[1]The University of Tokyo, 5-1-5 Kashiwanoha, Kashiwa, Chiba, 277-8561, Japan, ohnishi@hflab.k.u-tokyo.ac.jp, fujimoto@k.u-tokyo.ac.jp

[2]Nikon Corporation, 47-1, Nagaodaityou, Sakae, Yokohama, 244-8533, Japan, koichi.sakata@nikon.com, kazuhiro.suzuki@nikon.com, kazuaki.saiki@nikon.com

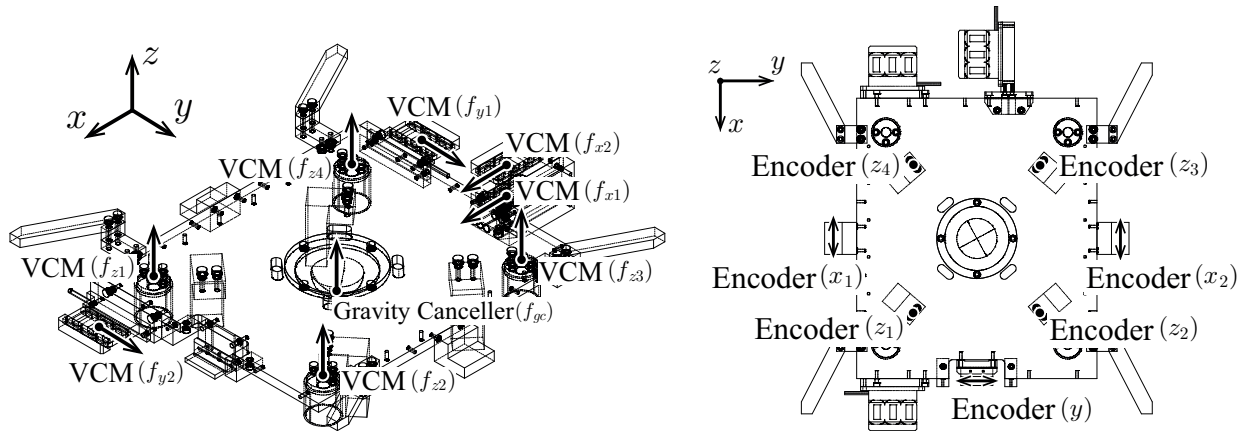

(a) Actuator arrangement of the fine stage.

(b) Sensor arrangement of the fine stage.

Fig. 3. Structure of the fine stage.

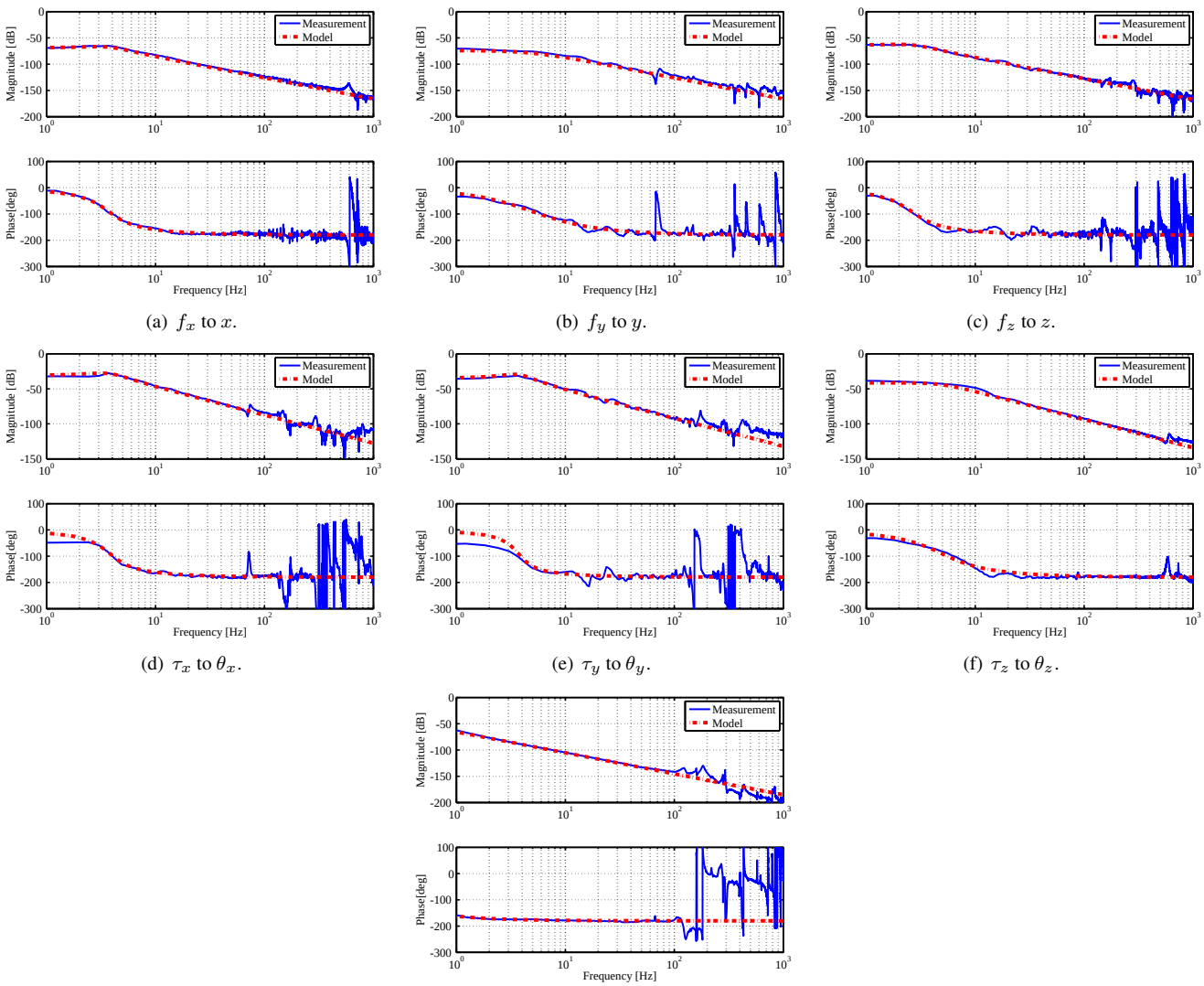

(a) f_x to x.

(b) f_y to y.

(c) f_z to z.

(d) τ_x to θ_x.

(e) τ_y to θ_y.

(f) τ_z to θ_z.

(g) f_X to X.

Fig. 4. Frequency responses of 6-DOF high-precision stage

control but also attitude control is important. Rotational motion, originally, has nonlinearity and coupling arising from rotational dynamics and kinematics. These effects could deteriorate the attitude control performance if a linear feedback and/or feedforward control is used. In recent studies, our research group proposed a nonlinear multi-input multi-output (MIMO) feedforward attitude controller which compensates for such effects [6]. In this paper, experiments are performed by using a new experimental 6-DOF stage to show the advantage of the attitude controller.

II. Experimental system

A. Structure of the high-precision stage

Our research group designed and fabricated an experimental 6-DOF high-precision stage shown in Fig. 1. The 6-DOF stage consists of a fine stage and a coarse stage, where the coarse stage has 1-DOF (X) and the fine stage has 6-DOF $(x, y, z, \theta_x, \theta_y, \theta_z)$. Two linear motors shown in Fig. 1 propel the coarse stage over long stroke. The fine stage is supported by 6-DOF air bearing called "gravity canceller" shown in Fig. 2.

By numerical analysis, the inertia tensor $\boldsymbol{I}_0$, taken at the fine stage's center of mass, is

$$\boldsymbol{I}_0 = 0.16 \begin{bmatrix} 0.40 & 0.024 & 0.0019 \\ 0.024 & 0.62 & 0.00090 \\ 0.0019 & 0.00090 & 1.0 \end{bmatrix} [\mathrm{kgm}^2]. \quad (1)$$

B. Gravity canceller

A picture and schematic of the gravity canceller is shown in Fig. 2. The gravity canceller compensates for the fine stage's gravity and supports 6-DOF without friction and it is composed of three parts: air gyro, planar air bearing and air bearing actuator which support $(\theta_x, \theta_y, \theta_z)$, (x, y) and (z) direction. The air bearing actuator also generates force f_{gc} in z direction to compensate for the gravity of the fine stage. An air compressor supplies about 0.4 MPa compressed air to each part of gravity canceller. Because the air compressor is located far from the stage, heat and vibration generated by the air compressor do not affect the stage.

C. Actuator and sensor arrangement

The actuator arrangement is illustrated in Fig. 3(a). The fine stage has eight VCMs which generate $(f_x, f_y, f_z, \tau_x, \tau_y, \tau_z)$. The sensor arrangement is shown in Fig. 3(b). The fine stage's position $(x, y, z, \theta_x, \theta_y, \theta_z)$ is measured by seven linear encoders and the distance between the fine stage and the coarse stage is measured by two laser sensors. Frequency responses are shown in Fig. 4, which are fitted by second-order transfer functions.

III. Attitude control model

A. Rotational dynamics

The model of the fine stage is illustrated in Fig. 5. The XYZ frame denotes the inertial frame and the xyz frame denotes the body-fixed frame with their origin at the center of mass of the fine stage. The rotational dynamics is described by Euler's equation, which is given by [7]

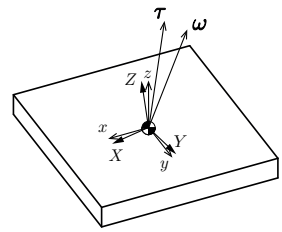

Fig. 5. Attitude control model.

$$\boldsymbol{\tau} = \boldsymbol{I}\dot{\boldsymbol{\omega}} + \boldsymbol{\omega} \times \boldsymbol{I}\boldsymbol{\omega}, \quad (2)$$

where $\boldsymbol{\tau} = [\tau_x, \tau_y, \tau_z]^{\mathrm{T}}$ denotes the control torque vector, $\boldsymbol{\omega} = [\omega_x, \omega_y, \omega_z]^{\mathrm{T}}$ denotes angular velocity vector, and $\boldsymbol{I}$ denotes the inertia tensor matrix defined as

$$\boldsymbol{I} = \begin{bmatrix} I_{xx} & I_{xy} & I_{xz} \\ I_{yx} & I_{yy} & I_{yz} \\ I_{zx} & I_{zy} & I_{zz} \end{bmatrix}, \quad (3)$$

with respect to inertial frame. Here, $\boldsymbol{I}$ is calculated by

$$\boldsymbol{I} = \boldsymbol{R}\boldsymbol{I}_0\boldsymbol{R}^{\mathrm{T}}, \quad (4)$$

where $\boldsymbol{R}$ is the rotation matrix of the body-fixed frame relative to the inertial frame and $\boldsymbol{I}_0$ is inertia tensor matrix when $\boldsymbol{R}$ is the identity matrix $\boldsymbol{E}$. In this paper, $\boldsymbol{R}$ is expressed by Z-Y-X Euler angle $\boldsymbol{\theta} = [\theta_x, \theta_y, \theta_z]^{\mathrm{T}}$:

$$\boldsymbol{R}(\theta_x, \theta_y, \theta_z) = \begin{bmatrix} \mathrm{c}\theta_z\mathrm{c}\theta_y & -\mathrm{s}\theta_z\mathrm{c}\theta_x + \mathrm{c}\theta_z\mathrm{s}\theta_y\mathrm{s}\theta_x & \mathrm{s}\theta_z\mathrm{s}\theta_x + \mathrm{c}\theta_z\mathrm{s}\theta_y\mathrm{c}\theta_x \\ \mathrm{s}\theta_z\mathrm{c}\theta_y & \mathrm{c}\theta_z\mathrm{c}\theta_x + \mathrm{s}\theta_z\mathrm{s}\theta_y\mathrm{s}\theta_x & -\mathrm{c}\theta_z\mathrm{s}\theta_x + \mathrm{s}\theta_z\mathrm{s}\theta_y\mathrm{c}\theta_x \\ -\mathrm{s}\theta_y & \mathrm{c}\theta_y\mathrm{s}\theta_x & \mathrm{c}\theta_y\mathrm{c}\theta_x \end{bmatrix}, \quad (5)$$

where s and c are the abbreviation of $\sin$ and $\cos$, respectively. Expanding the right-hand side of (2), Euler's equation can also be expressed as

$$\begin{bmatrix} \tau_x \\ \tau_y \\ \tau_z \end{bmatrix} = \begin{bmatrix} I_{xx}\dot{\omega}_x \\ I_{yy}\dot{\omega}_y \\ I_{zz}\dot{\omega}_z \end{bmatrix} + \begin{bmatrix} I_{xy}\dot{\omega}_y + I_{xz}\dot{\omega}_z \\ I_{yx}\dot{\omega}_x + I_{yz}\dot{\omega}_z \\ I_{zx}\dot{\omega}_x + I_{zy}\dot{\omega}_y \end{bmatrix} + \begin{bmatrix} I_{zz}\omega_y\omega_z \\ I_{xx}\omega_x\omega_z \\ I_{yy}\omega_x\omega_y \end{bmatrix} - \begin{bmatrix} I_{yy}\omega_y\omega_z \\ I_{zz}\omega_x\omega_z \\ I_{xx}\omega_x\omega_y \end{bmatrix} + \begin{bmatrix} I_{zx}\omega_x\omega_y + I_{zy}\omega_y^2 - I_{yx}\omega_x\omega_z - I_{yz}\omega_z^2 \\ I_{xy}\omega_y\omega_z + I_{xz}\omega_z^2 - I_{zx}\omega_x^2 - I_{zy}\omega_x\omega_y \\ I_{yx}\omega_x^2 + I_{yz}\omega_x\omega_z - I_{xy}\omega_y^2 - I_{xz}\omega_y\omega_z \end{bmatrix}. \quad (6)$$

Equation (6) indicates that Euler's equation has nonlinearity and coupling arising from the products of inertia and $\boldsymbol{\omega} \times \boldsymbol{I}\boldsymbol{\omega}$.

B. Rotational kinematics

Because of coordinate rotation, rotational motion has nonlinearity and coupling. Euler angle $\boldsymbol{\theta} = [\theta_x, \theta_y, \theta_z]^{\mathrm{T}}$ cannot be calculated by integrating the angular velocity $\boldsymbol{\omega} = [\omega_x, \omega_y, \omega_z]^{\mathrm{T}}$ linearly [8].

The derivative of rotation matrix $\dot{\boldsymbol{R}}$ is given by [7]

$$\dot{\boldsymbol{R}} = [\boldsymbol{\omega}\times]\boldsymbol{R}. \tag{7}$$

The notation $[\boldsymbol{\omega}\times]$ is the skew symmetric matrix formed from angular velocity $\boldsymbol{\omega} = [\omega_x, \omega_y, \omega_z]^{\mathrm{T}}$,

$$[\boldsymbol{\omega}\times] \equiv \begin{bmatrix} 0 & -\omega_z & \omega_y \\ \omega_z & 0 & -\omega_x \\ -\omega_y & \omega_x & 0 \end{bmatrix}. \tag{8}$$

To solve (7), the following equation is obtained:

$$\boldsymbol{R}(t) = e^{[\boldsymbol{\omega}\times]t} = \boldsymbol{E} + [\boldsymbol{\omega}\times]t + \frac{([\boldsymbol{\omega}\times]t)^2}{2!} + \dots \tag{9}$$

where t denotes time. By Rodrigues' rotation formula, $e^{[\boldsymbol{\omega}\times]t}$ can be written as

$$e^{[\boldsymbol{\omega}\times]t} = \boldsymbol{E} + [\boldsymbol{a}\times]\sin(\omega t) + [\boldsymbol{a}\times]^2(1-\cos(\omega t)), \tag{10}$$

where $\boldsymbol{E}$ denotes the 3×3 identity matrix. Here, $\boldsymbol{a}$ and ω are defined as

$$\boldsymbol{\omega} = \boldsymbol{a}\omega,\ \ \omega \equiv ||\boldsymbol{\omega}||_2,\ \ ||\boldsymbol{a}||_2 = 1. \tag{11}$$

Equation (9) shows that the rotational kinematics has nonlinearity and coupling.

IV. Conventional feedforward controller design

A. Linearization for rotational dynamics

Since the principal axes of inertia do not correspond with the control axes, the products of inertia are not zero generally. For linearization, however, it is usually assumed that the products of inertia and angular velocities are small and neglectable:

$$\begin{bmatrix} I_{xx} & I_{xy} & I_{xz} \\ I_{yx} & I_{yy} & I_{yz} \\ I_{zx} & I_{zy} & I_{zz} \end{bmatrix} \simeq \begin{bmatrix} I_{xx} & 0 & 0 \\ 0 & I_{yy} & 0 \\ 0 & 0 & I_{zz} \end{bmatrix}, \tag{12}$$

$$\omega_x\omega_y \simeq 0,\ \ \omega_y\omega_z \simeq 0,\ \ \omega_z\omega_x \simeq 0. \tag{13}$$

Applying the above approximations, (6) becomes

$$\begin{bmatrix} \tau_x \\ \tau_y \\ \tau_z \end{bmatrix} \simeq \begin{bmatrix} I_{xx}\dot{\omega}_x \\ I_{yy}\dot{\omega}_y \\ I_{zz}\dot{\omega}_z \end{bmatrix}. \tag{14}$$

Equation (14) shows that the relationship between $\boldsymbol{\tau}$ and $\dot{\boldsymbol{\omega}}$ is linearized.

B. Linearization for rotational kinematics

Because of coordinate rotation, rotational kinematics has nonlinearity and coupling as shown in section III. B. Here, ignoring coordinate rotation, the relationship between $\boldsymbol{\theta}$ and $\boldsymbol{\omega}$ is simplified as follows

$$\begin{bmatrix} \theta_x \\ \theta_y \\ \theta_z \end{bmatrix} \simeq \begin{bmatrix} \int \omega_x dt \\ \int \omega_y dt \\ \int \omega_z dt \end{bmatrix}. \tag{15}$$

Equation (15) shows that the relationship between $\boldsymbol{\theta}$ and $\boldsymbol{\omega}$ is linearized.

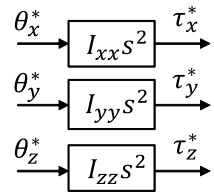

Fig. 6. Block diagram of the conventional FF.

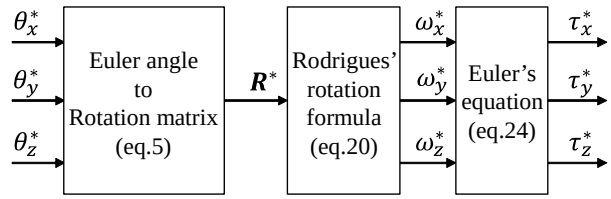

Fig. 7. Block diagram of the proposed FF.

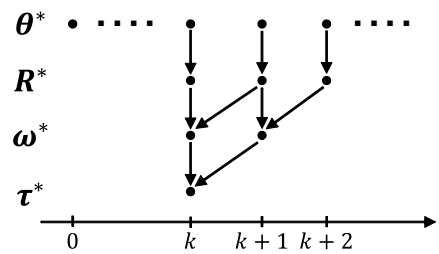

Fig. 8. Timing diagram of the proposed FF controller.

C. Design of conventional feedforward controller

Applying linearization for rotational dynamics and kinematics, which is described as (12), (13) and (15), Euler's equation (6) becomes

$$\begin{bmatrix} \tau_x \\ \tau_y \\ \tau_z \end{bmatrix} \simeq \begin{bmatrix} I_{xx}\ddot{\theta}_x \\ I_{yy}\ddot{\theta}_y \\ I_{zz}\ddot{\theta}_z \end{bmatrix}. \tag{16}$$

Using the Laplace transform for (16), the conventional feedforward controller is obtained.

$$\begin{bmatrix} \dfrac{\tau_x(s)}{\theta_x(s)} \\ \dfrac{\tau_y(s)}{\theta_y(s)} \\ \dfrac{\tau_z(s)}{\theta_z(s)} \end{bmatrix} = \begin{bmatrix} I_{xx}s^2 \\ I_{yy}s^2 \\ I_{zz}s^2 \end{bmatrix}. \tag{17}$$

The block diagram of the conventional feedforward controller is shown in Fig. 6.

V. Proposed feedforward controller design

Our research group proposed a novel nonlinear MIMO feedforward attitude controller which compensates for the nonlinearity and coupling arising from both rotational dynamics and kinematics [6]. The block diagram of the proposed feedforward controller is shown in Fig. 7 and the timing diagram is illustrated in Fig. 8.

A. Reference attitude trajectory $\boldsymbol{\theta}^*[k]$ and reference rotation matrix $\boldsymbol{R}^*[k]$

First, $\boldsymbol{\theta}^*[k]$ is generated properly such as by five-order polynomials. Then, $\boldsymbol{\theta}^*[k]$ is converted into $\boldsymbol{R}^*[k]$ by (5).

B. Kinematics compensation: Reference angular velocity $\boldsymbol{\omega}^*[k]$ and $\boldsymbol{\omega}^*[k+1]$

Expressing (7) and (9) into discrete-time system, the following equation is obtained:

$$e^{[\boldsymbol{\omega}^*[k]\times]T_s} = \boldsymbol{R}^*[k+1]\boldsymbol{R}^{*-1}[k], \tag{18}$$

where T_s denotes sampling time. For simplicity, the right-hand side of (18) is denoted by

$$\boldsymbol{R}^*[k+1]\boldsymbol{R}^{*-1}[k] = \begin{bmatrix} R_{11} & R_{12} & R_{13} \\ R_{21} & R_{22} & R_{23} \\ R_{31} & R_{32} & R_{33} \end{bmatrix}. \tag{19}$$

Then, according to (10) and (18), $\boldsymbol{\omega}^*[k]$ is given by

$$\boldsymbol{\omega}^*[k] = \begin{cases} [0\ 0\ 0]^{\mathrm{T}}, & \text{if } \boldsymbol{R} = \boldsymbol{E}, \\ \dfrac{\phi}{2T_s \sin\phi} \begin{bmatrix} R_{32} - R_{23} \\ R_{13} - R_{31} \\ R_{21} - R_{12} \end{bmatrix}, & \text{if } \boldsymbol{R} \neq \boldsymbol{E}, \end{cases} \tag{20}$$

where ϕ is given by

$$\phi = \cos^{-1}\left(\frac{R_{11} + R_{22} + R_{33} - 1}{2}\right). \tag{21}$$

$\boldsymbol{\omega}^*[k]$ realizes rotation between $\boldsymbol{R}[k]$ and $\boldsymbol{R}[k+1]$ using Euler axis. Therefore, nonlinearity and coupling of rotational kinematics are avoided. In the same way, $\boldsymbol{\omega}^*[k+1]$ is obtained from $\boldsymbol{R}^*[k+2]$ and $\boldsymbol{R}^*[k+1]$.

In addition, $\boldsymbol{I}$ used in (24) is obtained by

$$\boldsymbol{I} = \boldsymbol{R}^*[k]\boldsymbol{I}_0\boldsymbol{R}^{*\mathrm{T}}[k]. \tag{22}$$

C. Dynamics compensation: Feedforward reference torque $\boldsymbol{\tau}^*[k]$

Euler integral is given by

$$\boldsymbol{\omega}[k+1] = \boldsymbol{\omega}[k] + \dot{\boldsymbol{\omega}}[k]T_s. \tag{23}$$

According to (2) and (23), following equation is obtained:

$$\boldsymbol{\tau}^*[k] = \frac{1}{T_s}\boldsymbol{I}(\boldsymbol{\omega}^*[k+1] - \boldsymbol{\omega}^*[k]) + \boldsymbol{\omega}^*[k] \times \boldsymbol{I}\boldsymbol{\omega}^*[k]. \tag{24}$$

From the above equations, the feedforward reference torque $\boldsymbol{\tau}^*[k]$ is calculated, which can compensate for the nonlinearity and coupling arising from both rotational dynamics and kinematics.

VI. Experiment

A. Experimental conditions

Initial attitude is set as

$$\boldsymbol{\theta}[0] = \begin{bmatrix} 300 & -300 & 0 \end{bmatrix}^{\mathrm{T}}\ [\mu\mathrm{rad}], \tag{25}$$

and the reference attitude trajectories are given by 5-order polynomials, which are shown in Fig. 9. The sampling time T_s of the DSP is set as 200 μs.

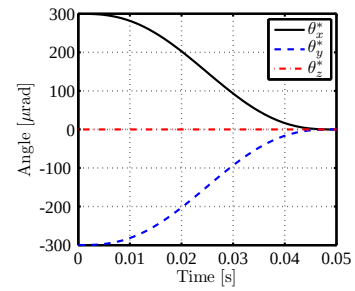

Fig. 9. Reference attitude trajectories.

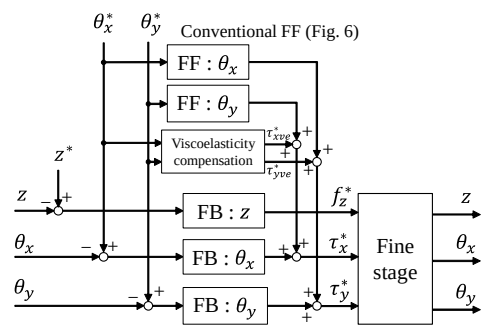

Fig. 10. Block diagram of the conventional controller (conventional FF + FB).

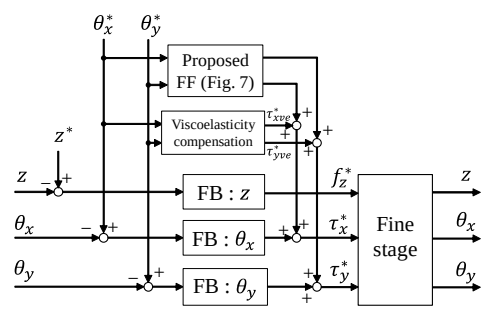

Fig. 11. Block diagram of the proposed controller (proposed FF + FB).

B. Controller design

The block diagram of the conventional controller and the proposed controller are shown in Fig. 10 and Fig. 11, respectively. Note that both 2-DOF controllers have the same PID feedback controllers. The PID feedback controllers are designed by pole assignment. The bandwidths of position loops are 20 Hz, 15 Hz and 15 Hz for the translation z, the rotation θ_x and θ_y, respectively. Fig. 4 shows that the plants have viscoelasticity. Therefore, the viscoelasticity is compensated by

$$\begin{bmatrix} \tau_{xve}^*[k] \\ \tau_{yve}^*[k] \end{bmatrix} = \begin{bmatrix} c_x\omega_x^*[k] + k_x(\theta_x^*[k] - \theta_x^*[0]) \\ c_y\omega_y^*[k] + k_y(\theta_y^*[k] - \theta_y^*[0]) \end{bmatrix} \tag{26}$$

in both the conventional controller and the proposed controller. Note that c_x and c_y denote coefficients of viscosity, and k_x and k_y denote coefficients of elasticity.

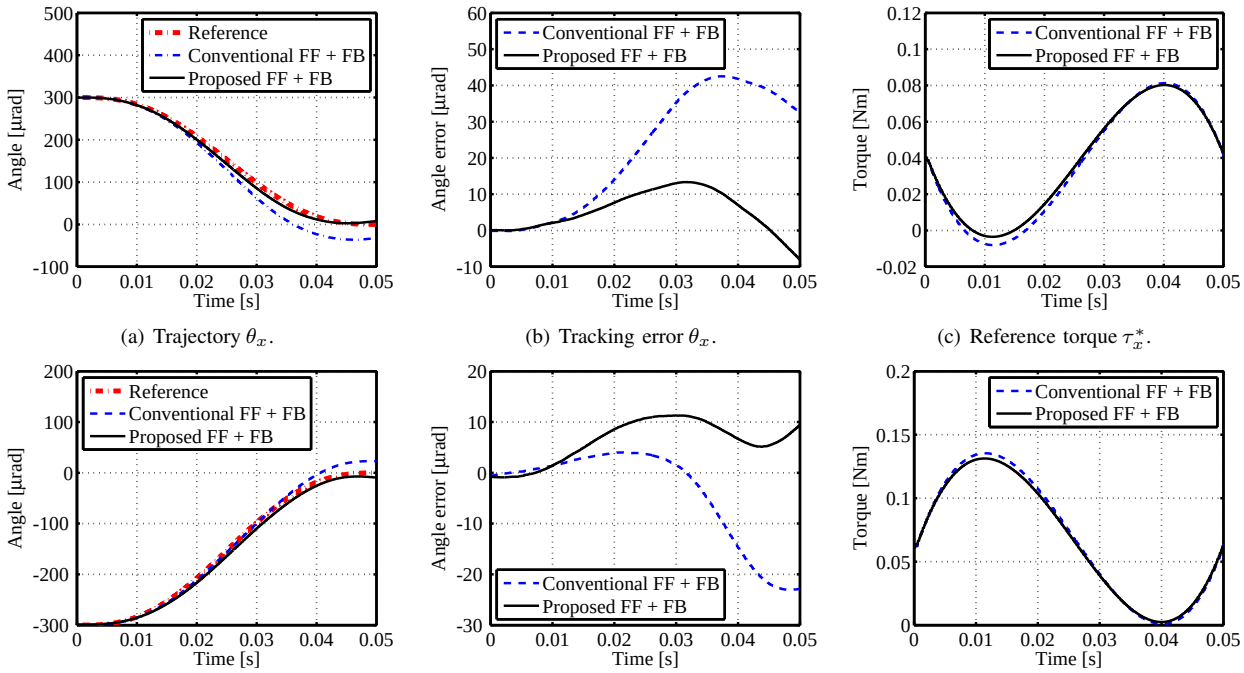

(a) Trajectory θ_x. (b) Tracking error θ_x. (c) Reference torque τ_x^*.

(d) Trajectory θ_y. (e) Tracking error θ_y. (f) Reference torque τ_y^*.

Fig. 12. Experimental results (FF + FB control).

TABLE I

EXPERIMENTAL RESULTS (FF + FB CONTROL). THE MAXIMUM VALUES OF TRACKING ERRORS.

	θ_x [μrad]	θ_y [μrad]
Conventional FF + FB	43	23
Proposed FF + FB	13	11

C. Experimental results

Experimental results are shown in Fig. 12 and listed in Tab. I. Fig. 12(a), and (d) show that the trajectories using the conventional controller exceed the reference trajectories. This result indicates that the trajectories are affected by the nonlinearity and coupling from other axes. Fig. 12(b), (e), and Tab. I show that the use of the proposed feedforward controller can improve the tracking performances 3.3 times for θ_x and 2.1 times for θ_y. Fig. 12(c), and (f) shows that $\boldsymbol{\tau}^*$ of the proposed controller is less than $\boldsymbol{\tau}^*$ of the conventional controller considering the nonlinearity and coupling.

From the above, the effectiveness of the proposed controller is verified through experiments.

VII. CONCLUSION

High-precision stages used in semiconductor and flat panel display manufacturing need to be controlled accurately in 6-DOF. 6-DOF stages require gravity compensation to suspend stages. In this paper, a new experimental 6-DOF high-precision stage with gravity canceller is designed and fabricated. This stage consists of a fine stage and a coarse stage. The gravity canceller compensates for the fine stage's gravity and supports 6-DOF without friction. This structure enables us to reduce heat which is generated close to the fine stage.

For attitude control, nonlinearity and coupling of rotational motion can deteriorate the attitude control performance. Finally, a MIMO feedforward attitude controller proposed in our past paper is applied to the new experimental stage. The advantage of the MIMO feedforward controller is shown by experiments.

REFERENCES

[1] T. Oomen, R. van Herpen, S. Quist, M. van de Wal, O. Bosgra, and M. Steinbuch, "Connecting System Identification and Robust Control for Next-Generation Motion Control of a Wafer Stage," *IEEE Trans. Control Systems Technology*, no. 99, pp. 1–17, 2013.

[2] H. Butler, "Position Control in Lithographic Equipment," *IEEE Control Systems Magazine*, vol. 31, no. 5, pp. 28–47, 2011.

[3] A. T. A. Peijnenburg, J. P. M. Vermeulen, and J. Van Eijk, "Magnetic levitation systems compared to conventional bearing systems," *Microelectronic engineering*, vol. 83, pp. 1372–1375, 2006.

[4] W. Gao, S. Dejima, H. Yanai, and K. Katakura, "A surface motor-driven planar motion stage integrated with an XYθZ surface encoder for precision positioning," *Precision Engineering*, vol. 28, no. 3, pp. 329–337, 2004.

[5] Y. Choi, and D. Gweon, "A High-Precision Dual-Servo Stage Using Halbach Linear Active Magnetic Bearings," *IEEE/ASME Trans. Mechatronics*, vol. 16, no. 5, pp. 925–931, 2011.

[6] W. Ohnishi, H. Fujimoto, K. Sakata, K. Suzuki and K. Saiki, "Proposal of Attitude Control for High-Precision Stage by Compensating Nonlinearity and Coupling of Euler's Equation and Rotational Kinematics," in *Proc. Int. Conf. IEEE IECON*, Nov. 2013.

[7] R. M. Murray, Z. Li and S. S. Sastry, "A Mathematical Introduction to Robotic Manipulation," CEC Press, 1994.

[8] I. Yamaguchi, T. Kida, O. Okamoto, and Y. Ookami, "Quaternion and Euler Angles in Kinematics," *Technical Memorandum of National Aerospace Laboratory*, vol. 636, pp. 1–15, 1991. (in Japanese)